Ternary Cathode Blend Electrodes for Environmentally Friendly Lithium-Ion Batteries

Nicola Michael Jobst,*[b] Alice Hoffmann,[b] Andreas Klein,[c] Stefan Zink,[b] and Margret Wohlfahrt-Mehrens[a]

The combination of two active materials into one positive electrode of a lithium-ion battery is an uncomplicated and cost-effective way to combine the advantages of different active materials while reducing the disadvantages of each material. In this work, the concept of binary blends is extended to ternary compositions. The combination of three different active materials provides high versatility in designing the properties of an electrode. Therefore, the unique properties of a layered oxide, phospho-olivine, and spinel type material are mixed to design a high-energy cathode with improved environmental friendliness. Four different compositions of blend electrodes are investigated, each with individual benefits. Synergistic effects improved the rate capability, power density, thermal and chemical stability simultaneously. The blend electrode consisting of 75% NMC, 12.5% LMFP and LMO provides similar energy and power density as a pure NMC electrode while economizing 25% cobalt and nickel.

Introduction

There is demand for high energy and high power density batteries because of the electrification of the mobility sector and the continuous development of powerful consumer electronics. Today, the desired performance is usually provided by lithium-ion batteries made from a graphite-based negative electrode and a positive electrode composed of a layered oxide, phospho-olivine, or spinel type intercalation material. However, the desired energy density, power density, safety, and price have not been achieved, mainly because of the properties of the cathode materials.[1–3] Layered oxides, namely $LiCoO_2$, $LiNi_xMn_yCo_zO_2$ (NMC, $x+y+z=1$) or $LiNi_xCo_yAl_zO_2$ (NCA, $x+y+z=1$), provide high capacity and energy density, average power density, and cycle life. However, they suffer from thermal instability, sensitivity to moisture, toxicity, and high raw material prices. The latter two are mainly caused by cobalt raw materials, which moreover is ethically critical because mining conditions often are unkown.[4,5] Despite high prices and the risk of a thermal runaway scenario, its high energy density makes it the most commonly used active material in state of the art lithium-ion batteries.[5,6] Phospo-olivines such as $LiFe_{1-x}Mn_xPO_4$ (LMFP, $x<1$) possess a strong phosphate-based backbone that provides high thermal and chemical stability. Hence, this cathode material is very convenient if high safety and high cycle life are required. As manganese and iron are both inexpensive and nontoxic raw materials, LMFP is significantly less expensive than layered oxides.[7–9] Although phospho-olivines provide satisfactory specific capacity and high rate capability, the low crystal density and high polarization are serious drawbacks that narrow possible application fields.[10,11] A third alternative of commercially available electrode materials are the spinel type materials such as $LiMn_2O_4$ (LMO). Fast kinetics promoted by three-dimensional diffusion paths through the crystal structure make them especially interesting for high power applications. However, a high power capability, satisfactory safety properties, and low price are accompanied by a rather low specific capacity and low energy density. The biggest disadvantage of manganese spinel materials is their chemical instability when in contact with an electrolyte. Manganese dissolution, strongly pronounced at elevated temperatures, leads to an impaired cycle life.[12,13]

The unique properties of these materials can be easily combined by physically mixing during slurry preparation. The combination of two different chemistries in one electrode is beneficial. The drawbacks of each component can be compensated by the advantages of the other, leading to an overall improved performance of the electrode. Liebmann et al. used a model system without intermixed particles to show that the currents applied during charge and discharge are inhomogenously distributed among the different electroactive materials.[14] Sup-

[a] Dr. M. Wohlfahrt-Mehrens
Zentrum für Sonnenenergie und Wasserstoffforschung Baden-Württemberg
Helmholzstraße 8, 89081 Ulm (Germany)
[b] N. M. Jobst, Dr. A. Hoffmann, S. Zink
Zentrum für Sonnenenergie und Wasserstoffforschung Baden-Württemberg
Lise-Meitner-Straße 24, 89081 Ulm (Germany)
E-mail: nicola.jobst@zsw-bw.de
[c] Dr. A. Klein
SGL Carbon AG
Werner-von-Siemensstraße 18, 86405 Meitingen (Germany)
Supporting Information and the ORCID identification number(s) for the author(s) of this article can be found under: https://doi.org/10.1002/cssc.202000251.

ported by simulation studies, the different working potentials result in significantly higher stress of one material at a given potential and the performance of the blend is negatively affected.[15] In contrast to these studies, blend electrodes are generally reported to show advantageous electrochemical performance. As frequently reported, particle–particle interactions of different active materials lead to synergistic effects within the electrode.[16,17]

The high demand for high energy density and high power capability makes the combination of NMC and LMO the most intensively investigated blend.[16–19] The specific capacity of these blends is lower compared with pure NMC, but the rate capability and power density is increased. Furthermore, the thermal stability is significantly improved and the exothermal heat generation is even lower than the linear combination of both materials. Additionally, manganese dissolution and the impaired cycle life induced by LMO is substantially reduced.[20–24] The addition of phospo-olivines such as $LiFePO_4$ also improve the rate capability of electrodes based on layered oxides. Moreover, the high thermal stability significantly improves the safety of the blend electrode.[25–30] Partial substitution of iron with manganese increases the energy density of the material, which enables both excellent electrochemical performance as well as low cost electrode when mixed with NMC.[29,30] The third binary combination, LMFP and LMO, is free of cobalt and nickel, which makes this blend inexpensive and environmentally friendly. The lithium redistribution between the two intercalation hosts entails a high pulse power capability.[10,32]

In this study, the concept of binary blend compositions is extended to ternary systems. The three most commonly used types of positive active materials are combined within one electrode. The synergistic effects of the binary combinations are expected to also occur in the ternary blend electrodes. As depicted in Figure 1, four blend compositions and three parent materials are investigated. Based on the voltage profiles of the parent materials, the performance of the blend electrodes is predicted. The comparison of the calculated and measured discharge curves reveals the occurrence of electrochemical synergistic effects. Further synergies are investigated with regard to their thermal and chemical stability towards a $LiPF_6$-based electrolyte.

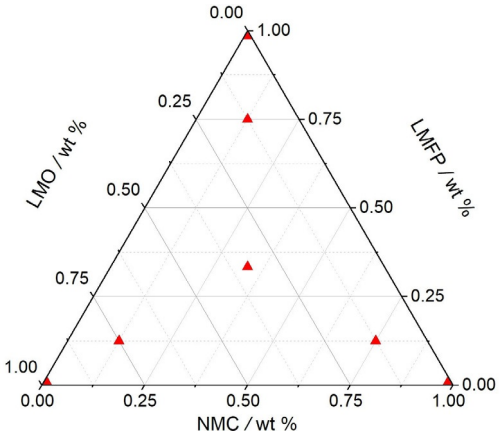

Figure 1. Compositions of the investigated active material in weight percentage.

Results and Discussion

The implications of three different active materials combined within one electrode were investigated. The composition of the four blend electrodes that were investigated are shown in the ternary mixing diagram in Figure 1. The given ratios are based on the total active material content of 93 %. In the case of the electrode 75 %NMC, the total active material comprises 75 % NMC, 12.5 % LMO, and 12.5 % LMFP. Relative to the total mass loading, including binder and conductive additives, the active material ratio of this electrode was 69.75 % NMC, 11.625 % LMFP and 11.625 % LMO. Three blend cathodes were chosen with a dominant share of one active material each. The electrochemical behavior and the chemical and thermal stability of these blend electrodes was mainly determined by one material. Therefore, it was possible to identify the properties and influence of each component on the electrochemical performance and chemical and thermal stability. The fourth blend electrode contained the same share of each material. By choosing these four compositions and characterizing the individual active materials, the whole matrix of the compositions was covered with a small number of samples. As NMC, LMO, and LMFP possess very different specific capacities and densities, the manufactured electrodes cannot be designed with the same mass loading, areal capacity, thickness, porosity, and density all at the same time. To produce the most comparable electrodes with respect to the rate capability, we decided to fix the areal capacity to 2.5 $mAh\,cm^{-2}$ and the porosity to 30 %. With the fixed areal capacity, all applied C-rates translate into the same current density, which results in the same electrochemical stress to all samples. Because it is impossible to realize the same electrode density with a practical value for all formulations, a fixed porosity of 30 % makes it possible to maintain a similar accessibility of electrolyte for all particles, especially as the particle sizes were very similar. The characteristic properties and labeling of the seven electrodes are listed in Table 1.

Electrochemical properties

The discharge profiles of all the blend electrodes at C-rates C/10 and 3 C are presented in Figure 2 and Figure 3. The reported specific capacities are calculated based on the active material content. Instead of displaying selected discharge profiles, each C-rate is represented as a mean value with standard deviation across three cycles. The discharge profiles of the blend electrodes are depicted in red. Additionally, the discharge profiles of each blend electrode were approximated using the proportionate sum of the parent materials' voltage profiles. To obtain them, the discharge curves of the single active materials were interpolated to 10 mV steps and summed up according to their weight percentage of the respective blend. This method has been thoroughly validated in the literature.[21,22] In

Table 1. Characteristic properties of electrodes with an areal capacity of approximately 2.5 mAh cm^{-2} and a porosity of 30% calculated from the electrodes' thickness. Mass loading includes active materials, binder, and conductive carbon. Specific capacity is based on 93% active material (AM) content. The proportions indicated in the second column are based on the total AM.

Label	NMC/LMFP/LMO [wt%]	Areal capacity [mAh cm^{-2}]	Mass loading [mg cm^{-2}]	Specific capacity [mAh g_{AM}^{-1}]	Porosity [%]	Density [g cm^{-3}]	Conductivity [S cm^{-2}]
100%NMC	100:0:0	2.51 ± 0.02	15.86 ± 0.07	170.14 ± 0.67	33 ± 2	2.83 ± 0.05	0.68 ± 0.11
100%LMFP	0:100:0	2.53 ± 0.04	17.89 ± 0.25	151.27 ± 0.30	32 ± 2	2.13 ± 0.03	1.16 ± 0.03
100%LMO	0:0:100	2.58 ± 0.02	26.25 ± 0.01	105.41 ± 0.08	31 ± 1	2.73 ± 0.02	0.39 ± 0.20
75%NMC	75:12.5:12.5	2.48 ± 0.01	16.07 ± 0.02	165.57 ± 0.12	32 ± 2	2.72 ± 0.04	1.84 ± 0.19
75%LFMP	12.5:75:12.5	2.46 ± 0.08	17.70 ± 0.55	149.25 ± 0.29	32 ± 2	2.27 ± 0.03	1.89 ± 0.19
75%LMO	12.5:12.5:75	2.59 ± 0.07	23.20 ± 0.28	118.49 ± 3.72	30 ± 2	2.70 ± 0.03	1.52 ± 0.19
33%each	33.3:33.3:33.3	2.41 ± 0.2	18.76 ± 0.65	136.45 ± 11.95	32 ± 2	2.54 ± 0.04	2.04 ± 0.20

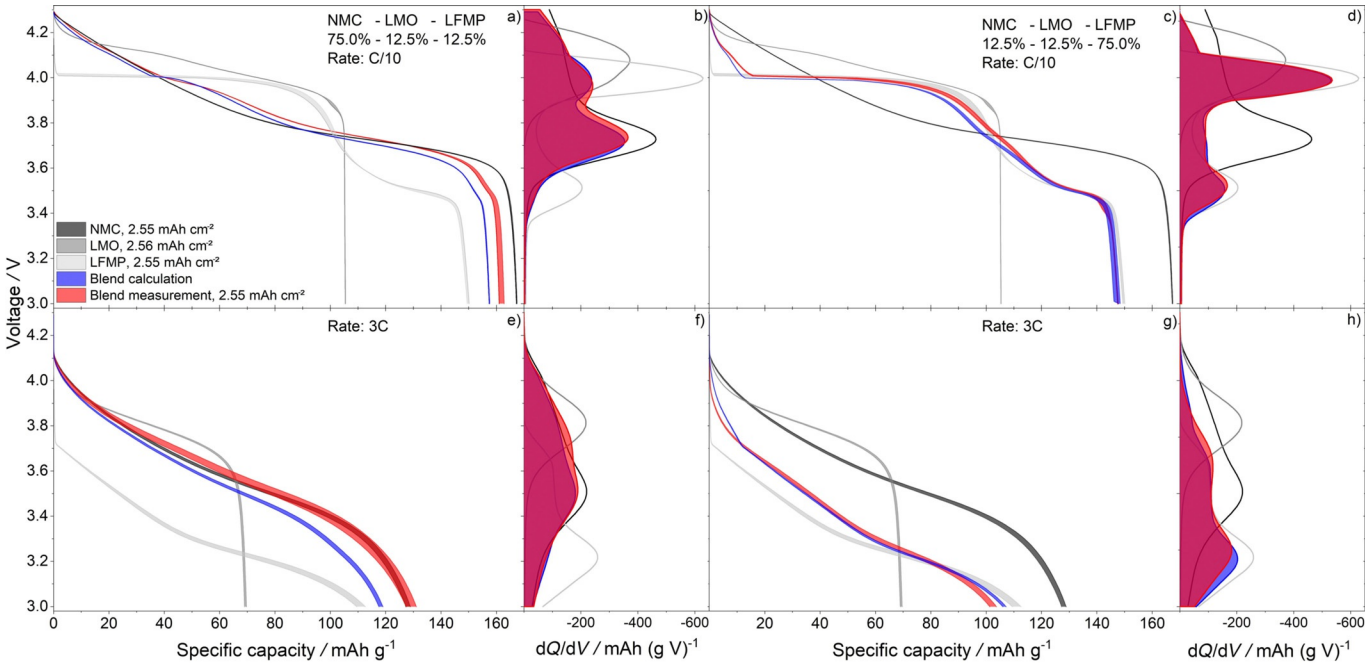

Figure 2. Discharge profiles with standard deviation across three cycles and their derivative of blend electrodes consisting of a, b, e, f) 75% NMC, 12.5% LFMP, and 12.5% NMC or c, d, g, h) 75% LFMP, 12.5% LMO, and 12.5% NMC depicted in red, the respective calculation in blue, and the individual active materials in shades of gray, measured at a C-rate of C/10 (top) and 3C (bottom).

the present study, this calculation is presented as a blue band created from the mean values and standard deviations of the potential profiles of the parent material electrodes. For direct comparison, the three single active material electrodes are depicted in gray color in each graph. The calculation provides a simple but reasonable prediction of the electrochemical behavior, neglecting any interactions and synergistic effects between NMC, LMFP, and LMO. To highlight the differences between blended electrodes, in which particles can interact, and the calculation if no interactions are considered, the differential capacity analysis of the mean values is presented to the right of each potential profile shown in Figure 2 and Figure 3. This function of the cell voltage shows a peak when the potential curve shows a plateau. Therefore, it offers high sensitivity to small changes in the discharge profile. This enables the identification of different active materials inside an electrode to a certain extent.[34]

The discharge profile of the reference electrode 100%NMC at C/10 is depicted as a black curve in Figures 2a, c and 3a and c. Within the voltage window from 4.3 to 3.61 V, it demonstrates the typical voltage slope known for layered oxides. At the end of discharge at 3.0 V, the electrode delivers a specific capacity of 170.1 mAh g^{-1}. The derivative of the capacity Q over voltage V, dQ/dV, reveals that the highest share of capacity is provided at 3.72 V. At a discharge rate of 3C (see Figures 2e, g, and 3e, g) a similar sloping potential is obtained. Because of polarization effects, the curve is shifted to lower voltages and delivers most of its capacity at a voltage 0.21 V lower compared with the discharge rate of C/10. The voltage drop towards the end of discharge is less pronounced, reaching a total specific capacity of 127.3 mAh g^{-1}. Two clearly separated voltage plateaus at C/10 were observed for the 100%LMFP electrode, depicted in gray color in Figures 2a,, 3a and c. Owing to the manganese plateau at 4.00 V and the iron plateau at 3.51 V, the derivative of the voltage curve in Figur-

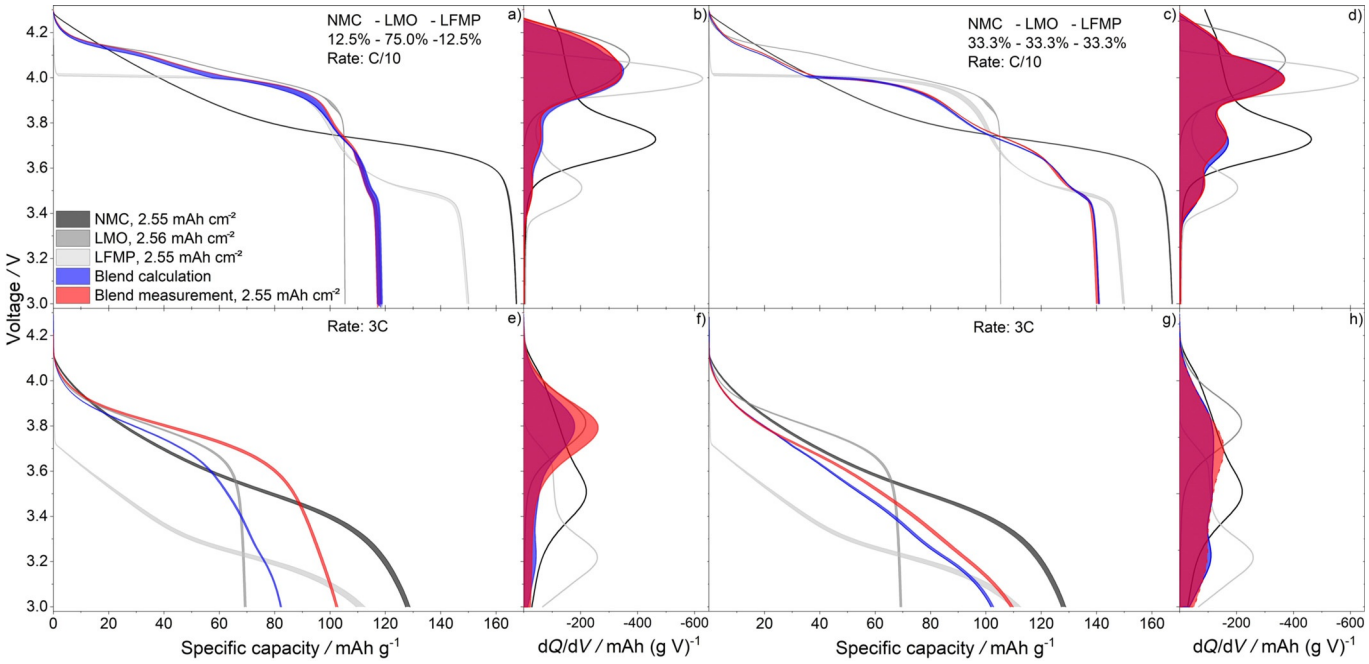

Figure 3. Discharge profiles with standard deviation across three cycles and their derivative of blend electrodes consisting of a, b, e, f) 75% LMO, 12.5% LFMP, and 12.5% NMC or c, d, g, h) 33.3% LFMP, 33.3% LMO, and 33.3% NMC depicted in red, the respective calculation in blue, and the individual active materials in shades of gray, measured at a C-rate of C/10 (top) and 3C (bottom).

es 2b, d, 3b, d shows two distinctly defined peaks. The total specific capacity of the electrode was 151.3 mAh g^{-1} at C/10. At a discharge rate of 3C (Figures 2e, g, 3e, g), the ohmic drop at the beginning of discharge was strongly pronounced, whereas the different oxidation states of LMFP are not easily distinguishable any more within the discharge profile. The derivative of the potential curve shows two merged peaks at 3.61 and 3.22 V.

Although most of the capacity at C/10 was provided at the voltage plateau of 4.00 V, the situation switched for the 3C curve, in which the peak in the voltage derivative at 3.22 V is more intense. At 3.0 V and a 3C discharge current, the 100%LMFP electrode provides a specific capacity of 112.7 mAh g^{-1}. The discharge profile of the 100%LMO electrode at a C-rate of C/10 is depicted in gray color in Figures 2a, c, 3a and 3c shows a gradual voltage decay from 4.30 to 3.92 V, followed by a steep voltage decline. Most of the electrode's total specific capacity of 105.4 mAh g^{-1} is provided above 4.08 V. At a C-rate of 3C (see Figure 2e, g, 3e, 3g), the slope of the discharge profile is much steeper and significantly shorter. The capacity provided by the electrode is reduced to a specific capacity of 69.7 mAh g^{-1}, which is mainly provided at 3.83 V as can be seen in the dQ/dV plot in Figures 2f, h and 3f, h. The pronounced ohmic drop and electrode polarization result from the high thickness of the electrode, which is caused by the low specific capacity of LMO and the areal capacity of 2.5 mAh cm^{-2}.

The discharge voltage profile of the 75%NMC electrode at a low C-rate is depicted in red in Figure 2a and b. Only small differences are evident between the observed and predicted values. At high voltages, the measured curve is close to the discharge profile of the 100%NMC electrode. At 4.0 V, a shoulder is formed, which can be assigned to the influence of LMO and the manganese plateau of LMFP stabilizing the voltage. The influence of LMFP is also observable towards the end of discharge. Here, a nearly linear voltage decrease occurs, which is most likely provided by the Fe^{2+}/Fe^{3+} voltage plateau. The measured blend electrode shows a lower polarization than calculated, throughout the discharge. As a result, the voltage drop towards the end of the discharge occurs later than calculated and the delivered capacity is 7.9 mAh g^{-1} higher than the estimated 157.7 mAh g^{-1}. In comparison with a pure NMC electrode, the blend provides only 4.4 mAh g^{-1} less capacity at C/10. The derivatives show the most prominent difference at approximately 3.8 V. The calculated discharge profile shows two peaks at 3.98 and 3.71 V. We attribute the first peak mainly to LMO and LMFP and the second peak to NMC. In the discharge profile of the measured 75%NMC electrode, the first peak of the dQ/dV plot is slightly downshifted to 3.96 V, whereas the second peak is shifted to a higher voltage of 3.72 V. Owing to the higher capacity contribution at approximately 3.8 V, the average voltage of the blend exceeds the calculated values as well as the values of the 100%NMC electrode.

At a discharge rate of 3C, the calculated and measured voltage curves already diverge at the beginning (see Figure 2e). The polarization of the electrode is lower than estimated and the blend electrode delivers approximately the same capacity as pure NMC. The overlap of the differential capacity analysis depicted in Figure 2f, shows that the capacity contribution at higher voltages is more pronounced in the case of the measured blend electrode compared with the calculated values or

pure NMC electrode, as indicated by the calculated blend capacity of 117.9 mAh g^{-1}. The 100 %NMC electrode delivered 128.0 mAh g^{-1} and the 75 %NMC electrode provided a capacity of 131.1 mAh g^{-1}.

The calculated discharge profile of the 75 %LMFP blend shown in Figure 2c matches well with the shape of the measured curve. The ohmic drop beginning at 4.3 V is slightly buffered by NMC and LMO. The change from the manganese to the iron plateau of LMFP is prolonged and shifted to higher voltages. Apart from these changes, the characteristics resemble those of the 100 %LMFP electrode. In addition, the measured discharge profile shows slightly higher voltages between 4.30 and 3.64 V relative to the calculated values. The derivative d*Q*/d*V* depicted in Figure 2d shows that the second voltage plateau of LMFP is slightly shifted to a higher voltage from 3.50 to 3.52 V. The overall specific capacity of the measured and the corresponding calculated value of the 75 %LMFP electrode was 149.3 mAh g^{-1}. At a discharge rate of 3 C, the capacity of the measured blend electrode provided 4.1 mAh g^{-1} less specific capacity than the calculated 106.7 mAh g^{-1}, as shown in Figure 2g. In contrast, the measured discharge profile showed higher voltages until 3.27 V. The calculations predicted the main capacity contribution at slightly lower voltages. The peaks in Figure 2h are at 3.21 and 3.26 V.

The discharge curve of the 75 %LMO electrode had the highest conformity with the proportionate sum of the parent materials' discharge curves at C/10. The derivative d*Q*/d*V* (Figure 3b) reveals a higher capacity contribution at high voltages for the measured blend compared with the calculated values and slightly less capacity below 4.0 V. Both had a specific capacity of 118 mAh g^{-1} at 3.0 V. At 3 C, the 75 %LMO electrode showed the biggest deviation to the calculated values of all investigated cases (Figure 3e).

Although the derivative d*Q*/d*V* does not reveal any voltage shifts (Figure 3f), which could be explained by polarization effects, significantly more capacity is contributed at 3.79 V. Compared with the capacity at C/10, this electrode loses only 13 % specific capacity at 3 C.

The discharge profile of the 33 %each electrode, presented in Figure 3c, originated from the same share of each active material. At a current of C/10, the differences between the calculated and measured voltage profiles are very small. Both curves show a specific capacity of 141.0 mAh g^{-1} at end of discharge. At low voltages, the voltage profile resembles the behavior of NMC and LMFP shown in Figure 2a for the 75 %NMC blend. Three peaks can be seen in the derivative of the calculated and measured voltage profiles (Figure 3d). Only the second peak at approximately 3.7 V deviates from the prediction. The experimental data reveal a higher capacity above 3.74 V, whereas the calculations predicted this capacity to be mainly provided below 3.71 V.

At a discharge rate of 3 C (Figure 3g and h), the contributions of the different active materials to the corresponding curves are no longer distinguishable. The blend electrode 33 %each provided most of its capacity at 3.70 V. The calculated d*Q*/d*V* curve does not show this peak, but proposes a nearly linear voltage decrease from 3.80 to 3.19 V. As a result, the blend electrode 33 %each delivered a higher specific capacity of 110.0 mAh g^{-1} instead of the estimated 103.0 mAh g^{-1}.

All blend electrodes revealed higher discharge voltages than those estimated by the calculations. Even if the capacity was slightly lower than predicted, as in the case of the 3 C discharge of the 75 %LMFP blend electrode, the average voltage was still higher than predicted. To determine whether the electric resistance is the reason for the reduced polarization, the apparent electronic conductivity was measured using a four-wire setup with two spring-loaded gold contacts with a contact area of 0.441 mm^2. The resulting electronic conductivity values of all blend electrodes appears to be significantly lower than the unblended electrodes (Table 1). Regardless of the composition, blended electrodes show two to three times higher conductivity than the parent material electrodes.

However, an explanation for the increased average voltage of the blend electrodes based on the higher conductivity lacks in completely elucidating the d*Q*/d*V* plots. If the conductivity of the 75 %LMO electrode was decisive for the improved performance, the peak in the d*Q*/d*V* plot would necessarily be found at a higher voltage compared with the calculated and higher than that for the pure LMO electrode. There must be an additional reason for the higher capacity contribution despite the same polarization. As already described in the literature, different active materials can redistribute lithium ions by diffusion from particle to particle.[10,35–36] Although the lithium redistribution occurs with electron exchange, this mechanism is probably only scarcely affected by the electrode polarization that originates from external currents. Therefore, it seems reasonable that the higher measured specific capacity of the blend electrodes compared with the calculated values is owed to the occurrence of lithium redistribution between different active material particles.

The areal capacity of 2.5 mAh cm^{-2} and the chosen porosity of 30 % have distinct implications on the comparability of the electrodes. Although the spinel-type material LMO is generally expected to provide a high rate capability, the 100 % LMO electrode suffered from strong polarization during the rate capability test (see Figure 2e). An LMO-based electrode with the same mass loading as the 100 %NMC electrode would be 34 μm thinner and therefore be affected by significantly less polarization at high current densities. The measurements and calculations presented in this section were additionally performed using a constant mass loading of 18 mg cm^{-2}. The results are shown in Figure S1 (Supporting Information) and demonstrate that the benefits of the blend electrodes are even more pronounced when the electrodes are manufactured to have the same mass loading.

Specific energy and energy density

A comparison of the specific energy, energy density, specific power and power density (at higher C-rates) of all the electrodes is shown in Figure 4. The energies were calculated from the electrode mass, taking the mass of the current collector into account. Additionally, the blue bars represent calculated

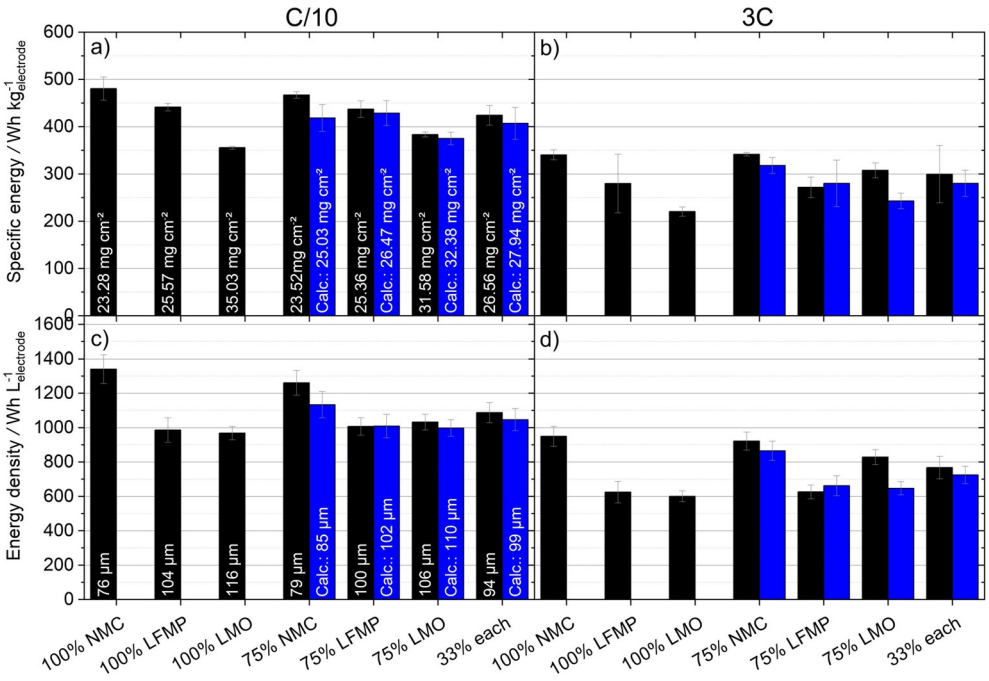

Figure 4. Specific energy and energy density of all investigated electrodes on electrode level discharged at C/10 (left) and 3C (right) represented as black bars. The red bars depict the values calculated from the proportionate sum of the parent materials.

energies obtained from the integrals of the calculated voltage profiles. The error bars were calculated from the standard deviation of three cells and three discharge energies per applied current. As expected, the specific energy increases with NMC content. However, the specific energies of the 75%NMC and 100%NMC electrodes are very similar. The blend electrode is the only one with a significantly higher specific energy than that calculated for C/10. The specific energies of all the other blend electrodes are within the standard deviation of the calculated values. At a higher C-rate, all blend electrodes delivered higher or equal specific energy densities in comparison with the estimated values. The 75%NMC and 100%NMC electrodes provided the highest specific power.

A similar behavior was found on the volumetric scale. The blend electrodes 75%LFMP, 75% LMO, and 33%each provided the expected energy density at a low C-rate, whereas the 75%NMC exceeded that of the calculated value. At a current corresponding to 3C, a higher energy density was found for the 75%NMC, 75%LMO, and 33%each electrodes. All blend electrodes exceeded the energy density of single active material electrodes 100%LMFP and 100%LMO at a current density of 3C. The blend 75%NMC electrode reached the energy density and specific energy of pure NMC also at a high C-rate of 3C.

Chemical stability

Transition metal dissolution from the active materials of the positive electrode into the electrolyte is one of several aging mechanisms typically observed for spinel-type electrodes.[17,37] To analyze the occurrence of this phenomenon, each of the investigated active material compositions (see Figure 1) was exposed to electrolyte for two weeks at 60 °C. The dissolution of transition metal into the electrolyte was quantified by analyzing the liquid by inductively coupled plasma optical emission spectrometry. Cobalt and nickel concentrations were under the detection limit. The manganese dissolution of all investigated electrodes is presented in Figure 5. With 16.5 mg kg^{-1} manganese dissolved from LMO into the electrolyte, the transition metal concertation was two orders of magnitude higher than for LMFP or NMC. By substituting 25% of the active material with NMC and LMFP, the detected amount of manganese was less than a tenth of the value obtained for pure LMO. Taking the values of all the electrodes into account, the concentration of manganese in the electrolyte and the concentration of LMO in the electrode seem to have an exponential correlation. Therefore, manganese dissolution occurred to a lower extent

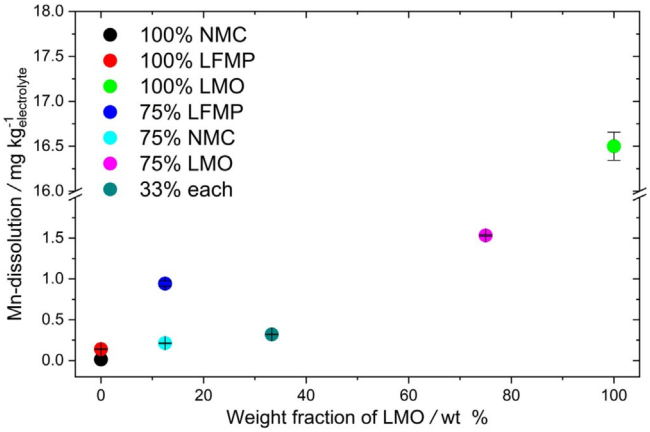

Figure 5. Manganese dissolution into the electrolyte after 2 weeks of soaking at 60 °C.

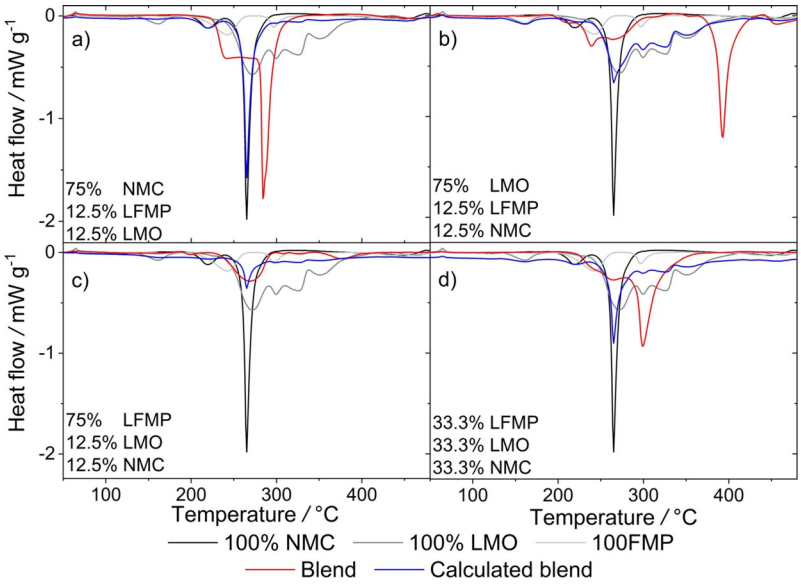

Figure 6. Differential scanning calorimetry of fully charged (4.3 V vs. Li/Li^+) blend electrodes (red), their parent material electrodes (gray), and the proportionate sum of the latter with respect to the displayed blend electrode.

than expected from the fraction of manganese spinel. This result is consistent with the findings from binary blend cathodes described in the literature.[10,21] The small amount of manganese dissolution lies within the magnitude of surface reactions only, which would imply that the lifetime of blend electrodes with LMO is less impaired than expected.

Thermal stability

The thermal stability of all cathodes was investigated by differential scanning calorimetry in the most unstable, fully charged state. The thermal behavior of the individual active material electrodes as well as the four blend electrodes and the respective cumulative calculation is shown in Figures 6a–d. Two small signals above 214 °C can be observed for 100 %LMFP, several unseparated reaction peaks above 231 °C are present for 100 %LMO and after a small reaction signal at 202 °C a sharp exothermal peak at 264 °C evolves in the case of 100 %NMC. The latter is associated with an oxygen release, which causes a high heat flux and critical thermal runaway scenario. The blend electrodes are neither described by the calculated curves nor resemble the respective main active material. However, one sharp peak can be seen in each graph of the blends 75 %NMC, 75 %LMO, and 33 %each in Figure 6a, b, and d, respectively. In comparison with the 100 %NMC electrode, this peak is shifted to a 20 and 36 °C higher temperature for 75 %NMC and 33 %each, respectively. In the blend electrodes containing 12.5 % NMC, this peak is at a similar position. For the 75 %LMO and 75 %LMF samples, the reaction reaches its peak at 393 °C and 379 °C, respectively. Similar to the manganese dissolution being a function of the LMO content, the position of the maximum heat flux resembles an exponential function of the NMC content. Owing to the unseparated reaction signals in most spectra, the true reaction heat is difficult to assess. However, the broad reaction ranges and the significantly delayed the main reaction, which we attribute to the decomposition of NMC, as indicated by a positive, synergistic effect on the safety of all blend electrodes. As expected, the 100 %LMFP electrode has the lowest reaction heat and the lowest heat flux.

Conclusions

$LiNi_xMn_yCo_zO_2$ (NMC), $LiFe_{1-x}Mn_xPO_4$ (LMFP), and $LiMn_2O_4$ (LMO) electrodes with an areal capacity of 2.5 mAh cm^{-2} and a porosity of 30 % were characterized. Based on this data, four ternary blend electrodes composed of a proportionate sum of these single active materials were modeled. Despite the simplicity of the calculation, the behavior of the manufactured blend electrodes was predicted very well, if the current density was low. At a higher current density of 3 C, only the discharge profile of the electrode consisting of 75 % LMFP, 12.5 % NMC, and 12.5 % LMO matched with the predicted behavior. For all other tested cases, the measured values of the blend electrode exceeded the calculated capacity or average voltage. Owing to the synergistic effects within the blend electrode, the energy densities were higher than estimated. One reason for the reduced polarization could be the electric conductivity of the electrodes. In fact, all blend electrodes had significantly higher conductivities than the single active material electrodes. As the particle sizes of all the materials were very similar, this observation can probably be explained by the general mixture rule.[38] However, the reduced polarization cannot be solely attributed to this property. Differential capacity analysis revealed a nonlinear shift of the capacity contributions during discharge. This indicated that the reduced polarization was predominantly promoted by synergistic effects that originated in different active materials in terms of a lithium redistribution.

Simple mixing of the different active materials does not completely eliminate the disadvantages of a single compo-

nent. In the first place, the high price of an NMC electrode can be reduced by adding a cheaper active material or the energy density of LMO is improved by adding a more energy dense material such as NMC. Secondly, synergistic effects can substantially reduce the drawbacks of each material. Adding a thermally stable compound such as LMFP can substantially reduce the threat of thermal runaway of a layered oxide. Manganese dissolution was still observed in mixtures with LMO, but it was reduced in an exponential relation. This was especially interesting as a small proportion of LMO significantly increased the rate capability. The combination of a material that provides a high energy density such as NMC, a safe material such as LMFP and a spinel material, which enables fast lithium-ion diffusion, results in a versatile mix of properties that can be freely designed for demanding applications.

The best overall performance was found for the blend consisting of 75% NMC, 12.5% LMFP, and 12.5% LMO. Compared with the single active material NMC, 25 wt% cobalt and 25 wt% nickel were economized, leading to a more cost-effective and ecological electrode. The transition metal dissolution of LMO was reduced by two orders of magnitude. With only 75% NMC in the blend, the specific capacity at a low discharge rate was slightly reduced, but the advantages of a higher energy density and power density compensate for this drawback. In fact, based on a porosity of 30%, the specific energy and energy density was similar to NMC utilized as individual material. DSC analysis indicated improved safety, as the decomposition of NMC was less dominant and significantly delayed. The trend towards the use of less thermally stable layered oxides such as NCA or nickel rich oxides makes this effect even more important. Within this study, it was shown for the first time that the concept of ternary cathode blend electrodes is a versatile method to effectively combine the advantages of very different active materials. Synergistic effects improve the electrochemical behavior, chemical, and thermal stability beyond the expected values.

Experimental Section

Electrode preparation

Seven different electrodes were prepared using the same formulation of 93 wt% active material, 4 wt% polyvinylidene fluoride (Solef PVdF 5130/1001, Solvay) binder, 2 wt% graphite (SFG6L, Timcal), and 1 wt% carbon black (SuperC65, Timcal). The active material content refers to the combination of $LiNi_{0.5}Mn_{0.3}Co_{0.2}O_2$ (BASF mean particle size 11.0 μm), $LiFe_{0.3}Mn_{0.7}PO_4$/C (Johnson Matthey Battery Materials GmbH, 150 mAh g^{-1}, mean particle size 10.0 μm, 3 wt% carbon coating), and $LiMn_{1.9}(Al,B)_{0.1}O_4$ (Toda America Inc., 105 mAh g^{-1}, mean particle size of 13.3 μm) as depicted in Figure 1. The active material compositions and the electrode properties are listed in Table 1. The slurry preparation was based on a solution of 7 wt% binder in N-methyl-2-pyrolidone (NMP). Graphite, carbon black, and the active materials were added and dispersed with a VMA-Getzmann Dispermat LC for a total time of 5 h. The resulting suspension was coated on aluminum foil using an automated thin film applicator (Elcometer 4340) and a doctor blade. The electrodes were dried for 2 h at 60 °C and at 80 °C overnight. The electrodes were manufactured with a target capacity of 2.5 mAh cm^{-2} and a porosity of 30%, to achieve highly comparable electrodes despite the very different properties. Porosity and density were calculated from crystal density and thickness measurements were performed with a thickness gauge. The electrode properties are listed in Table 1. The reported mass loadings are based on the whole composite, whereas the specific capacity is calculated on basis of the active material (AM) content.

Cell assembly

The electrochemical characterization was performed in a CR2016 coin cells (Hohsen) using two glass fiber (Whatman, GF/A) separators and 150 μL 1 M $LiPF_6$ in ethyl carbonate (EC) and ethyl methyl carbonate (EMC) (3:7), with 2 wt% vinylene carbonate (LP10-VC02, BASF) electrolyte, and a lithium metal counter electrode. The electrodes were dried at 130 °C for 12 h under vacuum prior to use. The cells were assembled in an argon-filled glovebox (MBraun, $O_2 < 0.1$ ppm, $H_2O < 0.1$ ppm).

Rate capability test

All electrodes with their different cell chemistries were cycled within the same voltage window of 3.0 to 4.3 V versus lithium metal counter electrode. After two cycles at a C-rate of C/10 and a potentiostatic step until a current corresponding to C/100 was reached, rate capability tests were performed at C/5, 1C, 2C, and 3C for 3 Cycles each. All electrochemical tests were performed on a BaSyTec CTS instrument at room temperature.

Electrolyte soaking test

The chemical stability of the active materials was analyzed by exposing the investigated composition to electrolyte. 60 wt% of the active materials were mixed with 30 wt% carbon black and 10 wt% PVdF binder dissolved in NMP. After drying, approximately 0.85 g of each mixture was placed into a pouch bag. Approximately 5 g electrolyte (BASF, EC/EMC = 3:7 *v/v* with 2% VC, 1 M $LiPF_6$) was added before sealing. After two weeks of storage at 60 °C, the electrolyte was extracted and diluted with ultrapure water to a total volume of 25 mL. This solution was analyzed with an inductive coupled plasma device ARCOS SOP (SPECTRO) with an optical emission sensor to evaluate the quantity of dissolved transition metal in the electrolyte.

Thermal stability test

The thermal stability of the fully charged electrodes (4.3 V) was investigated by DSC. The samples were extracted from T-cells (manufactured in house) after two cycles at C/10 charge and discharge rate with a CV step during charge, until a current corresponding to C/100 was reached. Inside an argon filled glovebox, the electrolyte was carefully removed before two 5 mm diameter electrodes were punched out and sealed inside a stainless-steel crucible. The DSC measurements were performed with a Netsch DSC 204 F1 (NETZSCH) instrument in the range from 30 to 520 °C with a heating rate of 5 °C min^{-1} under a nitrogen flow.

Acknowledgements

The results of this work have been obtained by the financial support of the "Bundesministerium für Bildung und Forschung"

within the Project Oekobat-2020 under the reference number 03XP0033F. We also want to thank Johnson Matthey Battery Materials GmbH for providing LMFP.

Conflict of interest

One of the investigated active materials, namely LMFP, was provided for free by the Johnson Matthey Battery Materials GmbH.

Keywords: batteries · blends · cathode · environmentally friendly · lithium

[1] T. Kim, W. Song, D.-Y. Son, L. K. Ono, Y. Qi, *J. Mater. Chem. A* **2019**, *7*, 2942 – 2964.
[2] B. Scrosati, J. Hassoun, Y.-K. Sun, *Energy Environ. Sci.* **2011**, *4*, 3287 – 3295.
[3] G. E. Blomgren, *J. Electrochem. Soc.* **2017**, *164*, A5019 – A5025.
[4] E. A. Olivetti, G. Ceder, G. G. Gaustad, X. Fu, *Joule* **2017**, *1*, 229 – 243.
[5] J. Xu, F. Lin, M. M. Doeff, W. Tong, *J. Mater. Chem. A* **2017**, *5*, 874 – 901.
[6] S. S. Zhang, *Energy Storage Mater.* **2020**, *24*, 247 – 254.
[7] K. Padhi, K. S. Nanjundaswamy, J. B. Goodenough, *J. Electrochem. Soc.* **1997**, *144*, 1188 – 1194.
[8] A. Lanjan, B. Ghalami Choobar, S. Amjad-Iranagh, *J. Solid State Electrochem.* **2020**, *24*, 157 – 171.
[9] K. Zaghib, A. Mauger, F. Gendron, M. Massot, C. M. Julien, *Ionics* **2008**, *14*, 371 – 376.
[10] A. Klein, P. Axmann, M. Wohlfahrt-Mehrens, *J. Power Sources* **2016**, *309*, 169 – 177.
[11] W. Liu, P. Gao, Y. Mi, J. Chen, H. Zhou, X. Zhang, *J. Mater. Chem. A* **2013**, *1*, 2411 – 2417.
[12] N. P. Pieczonka, Z. Liu, P. Lu, K. L. Olson, J. Moote, B. R. Powell, J.-H. Kim, *J. Phys. Chem. C* **2013**, *117*, 15947 – 15957.
[13] H.-W. Lee, P. Muralidharan, R. Ruffo, C. M. Mari, Y. Cui, D. K. Kim, *Nano Lett.* **2010**, *10*, 3852 – 3856.
[14] T. Liebmann, C. Heubner, C. Lämmel, M. Schneider, A. Michaelis, *ChemElectroChem* **2019**, *6*, 5728 – 5734.
[15] M. Kespe, S. Cernak, M. Gleiß, S. Hammerich, H. Nirschlet, *Int. J. Energy Res.* **2019**, *43*, 6762 – 6778.
[16] S. B. Chikkannanavar, D. M. Bernardi, L. Liu, *J. Power Sources* **2014**, *248*, 91 – 100.
[17] C. Heubner, T. Liebmann, M. Schneider, A. Michaelis, *Electrochim. Acta* **2018**, *269*, 745 – 760.
[18] S.-H. Wu, P.-H. Lee, *J. Power Sources* **2017**, *349*, 27 – 36.
[19] D. Wu, H. Ren, Y. Guo, X. Zhang, Z. Zhang, J. Li, *Ionics* **2019**, *25*, 1595 – 1605.
[20] E. Björklund, E. Wikner, R. Younesi, D. Brandell, K. Edström, *J. Energy Storage* **2018**, *15*, 172 – 180.
[21] T. Numata, C. Amemiya, T. Kumeuchi, M. Shirakata, M. Yonezawa, *J. Power Sources* **2001**, *97*, 358 – 360.
[22] J. Wang, Y. Yu, B. Li, P. Zhang, J. Huang, F. Wang, S. Zhao, C. Gan, J. Zhao, *ACS Appl. Mater. Interfaces* **2016**, *8*, 20147 – 20156.
[23] P. Gotcu, H. J. Seifert, *Phys. Chem. Chem. Phys.* **2016**, *18*, 10550 – 10562.
[24] S. Jung, *J. Power Sources* **2014**, *264*, 184 – 194.
[25] J. Whitacre, K. Zaghib, W. West, B. Ratnakumar, *J. Power Sources* **2008**, *177*, 528 – 536.
[26] C. Julien, A. Mauger, J. Trottier, K. Zaghib, P. Hovington, H. Groult, *Inorganics* **2016**, *4*, 17.
[27] K. G. Gallagher, S.-H. Kang, S. U. Park, S. Y. Han, *J. Power Sources* **2011**, *196*, 9702 – 9707.
[28] W.-J. Huang, J.-Y. Zheng, J.-J. Liu, R.-M. Yang, F.-X. Cheng, H.-B. Suo, H. Guo, S.-B. Xia, *J. Alloys Compd.* **2020**, *827*, 154296.
[29] J.-S. Lee, K. Heo, H.-S. Kim, M.-Y. Kim, J. Kim, S.-W. Kang, J. Lima, *J. Alloys Compd.* **2019**, *781*, 553 – 559.
[30] N. Besnard, A. Etiemble, T. Douillard, O. Dubrunfaut, P. Tran-Van, L. Gautier, S. Franger, J.-C. Badot, E. Maire, B. Lestriez, *Adv. Energy Mater.* **2017**, *7*, 1602239.
[31] X. Zhao, L. An, J. Sun, G. Liang, *J. Electrochem. Soc.* **2018**, *165*, A142.
[32] A. Klein, P. Axmann, M. Wohlfahrt-Mehrens, *J. Electrochem. Soc.* **2016**, *163*, A1936 – A1940.
[33] J. P. Schmidt, H. Y. Tran, J. Richter, E. Ivers-Tiffée, M. Wohlfahrt-Mehrens, *J. Power Sources* **2013**, *239*, 696 – 704.
[34] A. J. Smith, S. Smith, T. Byrne, J. Burns, J. Dahn, *J. Electrochem. Soc.* **2012**, *159*, A1696 – A1701.
[35] C. Heubner, C. Lämmel, M. Schneider, A. Michaelis, *J. Power Sources* **2017**, *344*, 170 – 175.
[36] T. Kobayashi, Y. Kobayashi, H. Miyashiro, *J. Mater. Chem. A* **2017**, *5*, 8653 – 8661.
[37] M. Saulnier, A. Auclair, G. Liang, S. Schougaard, *Solid State Ionics* **2016**, *294*, 1 – 5.
[38] J. Peltonen, M. Murtomaa, K. Robinson, J. Salonen, *Powder Technol.* **2018**, *325*, 228 – 233.

Manuscript received: January 30, 2020
Revised manuscript received: April 15, 2020
Accepted manuscript online: April 20, 2020
Version of record online: June 25, 2020

